Macromolecules

pubs.acs.org/Macromolecules Article

Bottlebrush Block Copolymer Assembly in Ultraconfined Films: Effect of Substrate Selectivity

Yaron Aviv, Esra Altay, Ofer Burg, Marcus Müller,* Javid Rzayev,* and Roy Shenhar*

Cite This: *Macromolecules* 2021, 54, 2079–2089 Read Online

ACCESS | Metrics & More | Article Recommendations | Supporting Information

ABSTRACT: Ultraconfined block copolymer films present nonbulk structures that are highly sensitive to film thickness and are strongly influenced by the wetting properties of the substrate. Here, we describe the self-assembly of bottlebrush block copolymers with varying side-chain lengths on different types of substrates. Our results show a pronounced influence of the nature of the substrate on the self-assembled morphology and the surface patterns that evolve during solvent−vapor annealing. In particular, we observe by experiments and simulations a transient, substrate-driven morphology of cylinder-like structures obtained in films of doubly symmetric (i.e., the backbone and side chains) bottlebrush block copolymers despite the general tendency of these polymers to form lamellar structures. The insights gained from this study highlight the ability to use the substrate chemistry for inducing the formation of unique morphologies in bottlebrush block copolymer films.

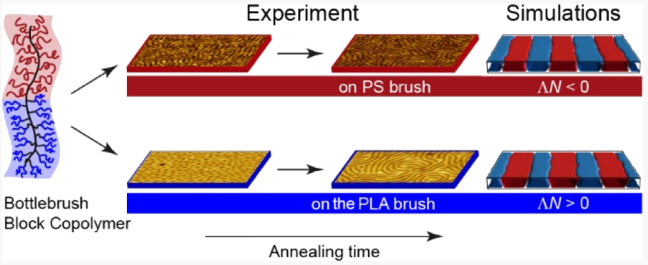

INTRODUCTION

Bottlebrush copolymers (BBCPs) represent an emerging class of branched macromolecules characterized by densely grafted polymeric side chains along a polymeric backbone.[1−3] Steric repulsion between the side chains results in elongated backbone conformations, decreased entanglements in the melt, and a strong tendency for forming alternating lamellae even with compositions that significantly deviate from symmetric.[4−14] Owing to their large molecular size and fast assembly dynamics,[15] bottlebrush block copolymers have facilitated access to periodic nanomaterials with large domain spacing for photonic applications.[11,14,16−18]

Unlike linear block copolymers, the composition in BBCPs (i.e., the volume fraction of each block) is dictated not only by the length of the backbone but also by the length of each type of graft. The graft lengths could be varied independently. Graft length asymmetry thus adds another knob that controls the equilibrium morphology of the BBCP. For example, a BBCP with asymmetric side chains can produce a cylindrical morphology upon self-assembly in the melt even when the backbone length of both blocks is similar.[19] Watkins et al. have reported the formation of a cylindrical morphology at a low volume fraction of the block bearing the shorter side chains.[13]

We have recently investigated the assembly of polystyrene−polylactide (PS−PLA) BBCPs of varying compositions in ultraconfined films on silicon wafers covered with native oxide.[20] The morphologies observed in this study corresponded to the expected bulk morphologies when confined to thin films. Nonetheless, it is well known that the morphologies of block copolymers in ultraconfined films are far richer than that in the melt,[21] featuring nonbulk morphologies and an extreme sensitivity to film thickness and substrate selectivity.[22−24] Modifying the substrate with a polymer brush enables controlling its wetting selectivity, which, in turn, influences domain orientation.[25] In this study, we reveal the unique morphological behavior that arises from the combination of the bottlebrush architecture, the ultraconfined film thickness, and the substrate chemistry.

RESULTS AND DISCUSSION

Two types of BBCPs with polymethacrylate backbones, PS grafts on one block, and PLA bifurcated grafts on the other were synthesized as previously reported (see the Experimental Section and the Supporting Information, Figure S1, for additional details).[11] Both polymers contained approximately symmetric backbone lengths and either symmetric or asymmetric lengths of the PS and PLA grafts (see Figure 1 and Table 1). The polymers were denoted according to the calculated volume fractions of the PLA-grafted blocks as $BBCP_{sym}$ (f_{PLA} = 43−46%) and $BBCP_{PLA\ maj}$ (f_{PLA} = 68%). Both types of BBCPs were assembled on three types of substrates: silicon wafers coated with native silicon oxide (denoted as "SiOx substrate") and similar wafers modified with PS and PLA brushes [denoted as "PS brush" and "PLA brush",

Received: September 5, 2020
Revised: February 2, 2021
Published: February 18, 2021

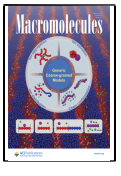

https://dx.doi.org/10.1021/acs.macromol.0c02057
Macromolecules 2021, 54, 2079−2089

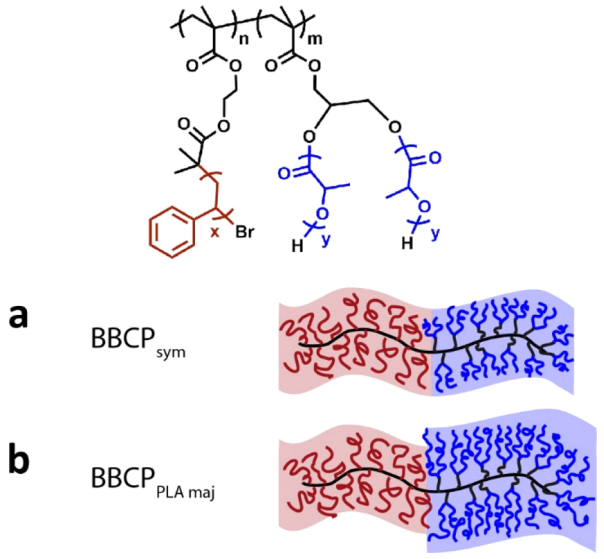

Figure 1. Chemical structures of (PGM-*graft*-PLA)-*block*-(PBIEM-*graft*-PS) BBCPs: (a) graft-symmetric $BBCP_{sym}$; (b) graft-asymmetric $BBCP_{PLA\ maj}$. See Table 1 for polymer characteristics.

respectively; see the Supporting Information, Figure S2, for a representative atomic force microscopy (AFM) imaging of the brush]. The surface energies of the SiOx substrate, the PS brush, and the PLA brush were calculated from contact angle measurements to be 73.7, 42.0, and 43.5 mJ/m^2, respectively (see the Supporting Information for additional details). All films were annealed under saturated tetrahydrofuran (THF) vapor, and microscopy images were taken at different intervals (1−60 min) along the annealing process.

Several considerations have to be taken into account regarding the selectivity of the substrate and annealing solvent to either block at the corresponding interfaces: the choice of film thickness and the implications that arise from the combination of these conditions. First, the PS brush and PLA brush are strongly selective to the PS and PLA domains of the BBCP film, respectively. Owing to the high incompatibility between PS and PLA ($\chi_{PS,PLA}$ = 0.32),[26] each of these substrates should exhibit a strong preference to one of the blocks in the copolymer. The SiOx substrate, in turn, is comparably nonpreferential (see the Supporting Information for additional details). Nonetheless, it is expected to show slight preference to the PLA-grafted blocks because of both surface tension considerations and the entropic contribution of their large number of PLA chain ends (owing to their bifurcated architecture), which increases their surface wetting tendency.

The annealing solvent (THF) is slightly PS-selective ($\chi_{THF,PS}$ = 0.15; $\chi_{THF,PLA}$ = 0.62).[27] This means that on a PS brush, the interfaces should display symmetric wetting conditions (i.e., PS domains are preferred at both interfaces), whereas on a PLA brush-coated substrate, the conditions imply antisymmetric wetting (i.e., PLA is preferred at the polymer/substrate interface, and PS is preferred at the free surface).

In this work, we were interested in studying the influence of the substrate selectivity in the case of ultrathin films, where the film thickness is considerably smaller than the radius of gyration of the BBCP. The total film thicknesses on all substrates were 15 nm (including a 5−6 nm thickness of the PS and PLA brushes), whereas the bulk periodicities (L_0) were 73 and 84 nm for $BBCP_{PLA\ maj}$ and $BBCP_{sym}$, respectively (determined by small-angle X-ray scattering).[20] This thickness confinement does not allow the BBCPs to accommodate fully developed parallel domains, which require the thickness to be at least $0.5L_0$. Hence, in this study, both blocks were forced to be present at the substrate interface, and the self-assembly should be regarded as quasi-two-dimensional (quasi-2D). Estimating the average cross-sectional diameter of the BBCPs to be in the range of 8−13 nm (following the works of Sheiko et al.[28] and Russell et al.[29]), we calculate that the ultrathin film thicknesses used in our work represent between one and two layers of BBCP chains lying flat on the surface.

Single-Chain Behavior above the Order−Disorder Transition. The experimental study was accompanied by molecular simulations of a soft, coarse-grained bottlebrush model to study the structure formation and (meta)stable morphologies of BBCPs in ultrathin films (see the Experimental Section for additional details). One of the hallmarks of the conformation of the bottlebrush architecture is the stretching of the backbone, which results from the crowding of the side chains that emanate from the backbone. We used the parameter η to quantify the ratio of the volume occupied by zN_{sc} side chains and the volume that corresponds to the unperturbed side-chain extension, $b_0(N_{sc})^{1/2}$ as follows[30]

$$\eta = zN_{sc}\frac{N_{sc}/\rho_0}{(b_0^2N_{sc})^{3/2}} = \frac{z\sqrt{N_{sc}}}{\rho_0 b_0^3} \approx \frac{z\sqrt{N_{sc}}}{11.9} \quad (1)$$

where z is the number of side chains attached to each backbone segment, b_0 denotes the statistical segment length, N_{sc} represents the number of segments of the side chain, and ρ_0 quantifies the segment number density (see model description in the Experimental Section). Here, we consider a fraction of the backbone that has the same number of segments as the side chains in order to count the number of segments inside the volume, $(b_0^2N_{sc})^{3/2}$. For large η, the backbone has to stretch due to the crowding of the side chains; this defines the proper bottlebrush regime. For the density values we used, the A block is at the crossover between the comb and bottlebrush, whereas the B block is more deeply in the bottlebrush regime.[30]

Table 1. Characteristics of the Bottlebrush Block Copolymers Used in This Study

			PS block[c]		PLA block[c]		
polymer notation	molecular weight, M_n (kDa)	polydispersity index, $Đ$	n	x	m	y	PS volume fraction, f_{PS}[d]
$BBCP_{sym}$	1439[a]	1.11	156	42	150	32	0.54
	1368[b]	1.15	151	43	150	29	0.57
$BBCP_{PLA\ maj}$	2130	1.09	143	40	150	70	0.32

[a]BBCPs used on SiOx substrates. [b]BBCPs used on the substrates modified with PS and PLA brushes. [c]The values of n, m, x, and y correspond to the number of backbone and graft repeat units according to Figure 1. [d]Volume fractions calculated based on the densities of PS and PLA.

https://dx.doi.org/10.1021/acs.macromol.0c02057
Macromolecules 2021, 54, 2079−2089

Figure 2a shows the time evolution of the mean-squared end-to-end distance of the bottlebrush's backbone in a thin

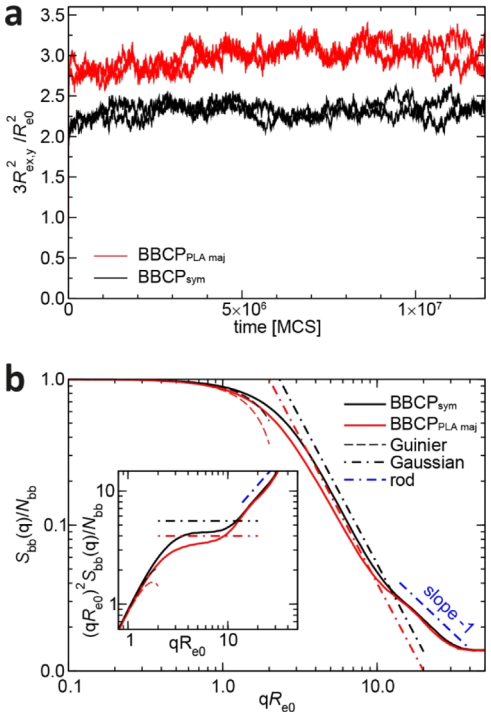

Figure 2. (a) Time evolution of the mean-squared lateral chain extension in a thin film of BBCP$_{sym}$ and BBCP$_{PLA\ maj}$ in the disordered state as a function of time, measured in MCS. Data represent the two lateral extensions. (b) 2D single-chain structure factor, $S_{bb}(q)$, calculated for the backbones of BBCP$_{sym}$ and BBCP$_{PLA\ maj}$ in a thin film, compared with the Guinier approximation, the Gaussian scale-free behavior, and the scattering of a rod. The inset shows the Kratky plot of $S_{bb}(q)$.

film during equilibration. The data are scaled to be comparable to the extension, R_{e0}, of a chain of length N_{bb}, that is, the bare backbone in a melt. We clearly observe that the backbone is stretched, that is, the square end-to-end distance, $R_e^2 = 3\langle R_{ex}^2\rangle = 2.28R_{e0}^2$ for BBCP$_{sym}$ and $3.00R_{e0}^2$ for BBCP$_{PLA\ maj}$. Additionally, the figure suggests that an equilibration time of 10^7 Monte Carlo steps (MCS) suffices to relax the conformations of these large polymers. In the disordered phase, the lateral self-diffusion constants of the center of mass, D, estimated from the displacement after at least $\Delta t = 6 \times 10^6$ MCS are $2.99 \times 10^{-8} R_{e0}^2$/MCS or $2.26 \times 10^{-8} R_{e0}^2$/MCS for BBCP$_{sym}$ or BBCP$_{PLA\ maj}$, respectively. The ratio of the self-diffusion coefficients, 1.32, is roughly comparable to the inverse ratio of the number of coarse-grained segments per BBCP, 1.46. Due to the correlation hole, however, the chains in the disordered melt interact, and the center-of-mass displacement deviates from the linear behavior predicted by the Rouse model for early times. In analogy to the Rouse model, nevertheless, we define a Rouse time of a bottlebrush by $\tau_{Rouse} \equiv 3\langle R_{ex}^2\rangle/(3\pi^2 D) \approx 2.6 \times 10^6$ MCS and 4.5×10^6 MCS for BBCP$_{sym}$ or BBCP$_{PLA\ maj}$, respectively. In the rest of the discussion, we measure all times in units of τ_{Rouse}.

To analyze the quasi-2D chain conformations in the disordered film, we present in Figure 2b the calculated structure factor of the backbone of the bottlebrushes, normalized by the number of backbone segments. The wave vector, $\mathbf{q}$, is parallel to the film surfaces. The small-angle scattering provides information about the radius of gyration of the backbone. In this generic Guinier regime, $S(\mathbf{q})/N_{bb} = 1 - \mathbf{q}^2 R_g^2/3 + O([\mathbf{q}^2 R_g^2]^2)$ defines radius of gyration, $R_g^2 = 3\langle R_{gx}^2\rangle = 3\langle R_{gy}^2\rangle$. At intermediate wave vectors, the scattering is compatible with the scale-free Gaussian chain behavior, $S(\mathbf{q})/N_{bb} \approx 12/[\mathbf{q}^2 R_e^2]$, with the mean-squared end-to-end distance, $R_e^2 = 3\langle R_{ex}^2\rangle = 3\langle R_{ey}^2\rangle$. For larger wave vectors, $S(\mathbf{q})/N_{bb}$ decays like $1/|\mathbf{q}|$, characteristic of the scattering of rod-like particles. The latter regime signals the stiffening of the backbone due to the crowding of the side chains. The values of R_e^2 and R_g^2, extracted from the segment coordinates, are employed for the asymptotic behavior in Figure 2b and are compiled in Table 2. The

Table 2. Stretching of the Bottlebrush Backbone in the Lateral Directions of the Film

	BBCP$_{sym}$	BBCP$_{PLA\ maj}$
$18\langle R_{gx}^2\rangle/R_{e0}^2$	2.23	2.88
$3\langle R_{ex}^2\rangle/R_{e0}^2$	2.28	3.00
$\lambda_{max}/\lambda_{min}$	5.18	5.51

large deviation from unity of the ratios between the measured chain extension of the bottlebrush in the film and that of the bare backbone in a melt quantifies the stretching of the BBCP chains in the film. The table also provides the ratio of the maximal and minimal eigenvalues of the 2D tensor of gyration of the molecular backbone, $\lambda_{max}/\lambda_{min}$, which represents the anisotropy of the instantaneous configuration of the backbone.[31]

Self-Assembly of the Symmetric BBCP. We first describe the self-assembly results of the BBCP$_{sym}$ system, which features a symmetric backbone as well as symmetric graft length compositions and thus serves as the bottlebrush analogue of symmetric linear block copolymers. On the PS brush, the film displays a pattern of short alternating stripes, which elongate over time (Figure 3a–d). Simulation results obtained after quenching the disordered system to $\chi N_{bb} = 36$ capture this behavior (Figure 4, top row). Using AFM phase images (insets in Figure 3) and the difference in Young's modulus between the PS and PLA domains (1270 and 1310 MPa, respectively[32]), we conclude that the PS domains (soft) appear as bright features in the AFM height images and as dark features in the scanning electron microscopy (SEM) images (see additional discussion below).[33]

The striped pattern is indicative of a lamellar morphology oriented perpendicularly to the substrate, which is consistent with the thickness restriction. Surface fraction analyses performed on the AFM images (see the Experimental Section for additional details) reveal that the surface fraction of the PS domains, σ_{PS}, did not change appreciably during the annealing process. The average value of σ_{PS} was 0.57 ± 0.04, which is the same as the PS volume fraction of BBCP$_{sym}$ used ($f_{PS} = 0.57$). However, considering that both interfaces are PS-selective (i.e., not neutral), it is reasonable to expect that the PS domains will be slightly expanded at both interfaces. This expectation was confirmed by the simulations, which show curved interfaces between the PS and PLA domains, where the PS domain boundaries are convex (Figure 5, top panel).

The structural evolution of BBCP$_{sym}$ on SiOx follows a similar path, starting from a pattern featuring worm-like PLA structures that fuse into stripes during annealing (Figure 3e–h). The PS fraction present at the film surface, averaged over

https://dx.doi.org/10.1021/acs.macromol.0c02057
Macromolecules 2021, 54, 2079–2089

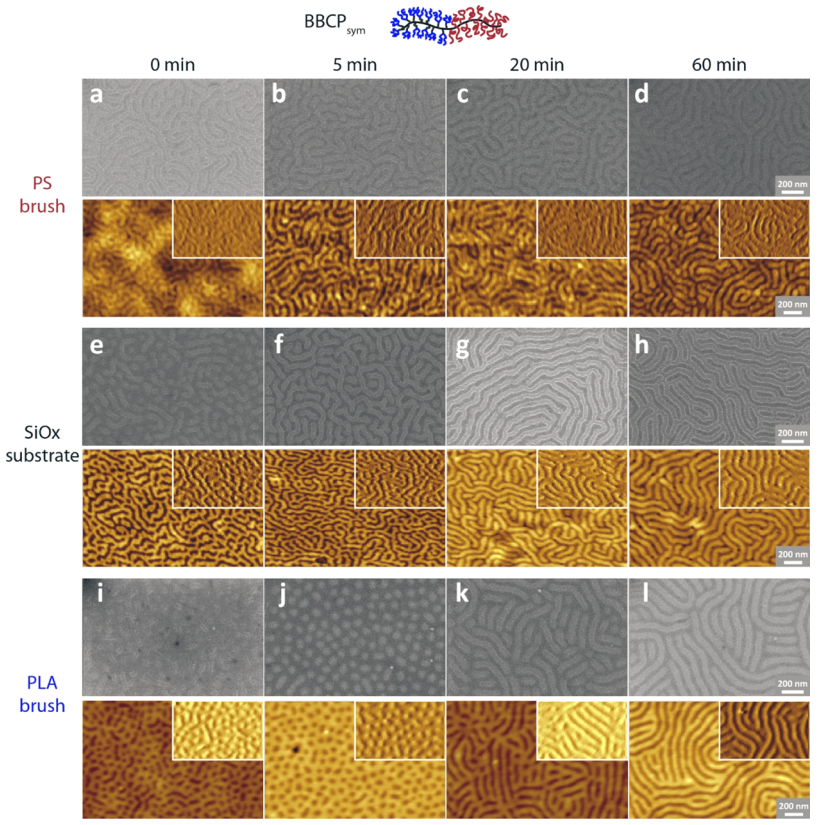

Figure 3. Self-assembly of $BBCP_{sym}$ in ultrathin films on three different types of substrates. Top: SEM images; bottom: AFM height images; insets: AFM phase images corresponding to the same portion of the height image it overlaps. AFM height *z*-scale: 15 nm.

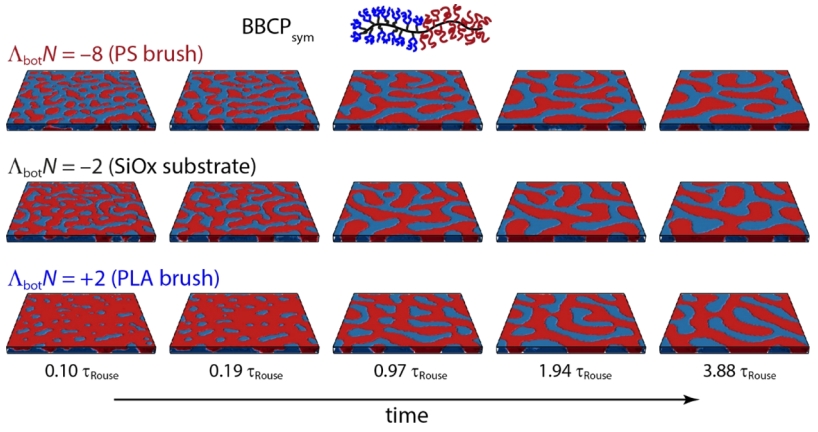

Figure 4. Simulation results showing the structure evolution in thin films of $BBCP_{sym}$ on various substrates. The *A* and *B* components (PS and PLA domains) are colored red and blue, respectively.

the course of annealing, was measured to be 0.52 ± 0.08, which is comparable to f_{PS} of the polymer batch used for the self-assembly on SiOx (f_{PS} = 0.54). The less ordered appearance of the initial structure compared to the as-cast structure of the same polymer cast on the PS brush is attributed to the difference in substrate selectivity. SiOx is rather nonselective, but the high number of PLA ends gives rise to an entropically driven substrate wetting. Hence, the polymer tends to direct the PLA grafts toward the substrate. As a result, PLA is depleted from the surface of the film, leading to worm-like PLA structures (instead of continuous stripes as observed on the PS brush). This conclusion is corroborated by the simulations (Figure 4, middle row), which show a higher exposure of the PS domains at the free surface and worm-like PLA structures. During annealing, the surface pattern of the film becomes similar to that observed on the PS brush-coated substrate.

The structural evolution suggests that upon casting, the immediate response of the BBCP film is to follow the substrate preference, whereas the influence of the polymer composition requires more time to be expressed in the film morphology. Nonetheless, the details of the three-dimensional (3D) morphology of the film cast on SiOx are expected to be different from that of the film cast on the PS brush because of the difference in wetting conditions (antisymmetric vs symmetric, respectively). Indeed, the simulations show that

https://dx.doi.org/10.1021/acs.macromol.0c02057
Macromolecules 2021, 54, 2079−2089

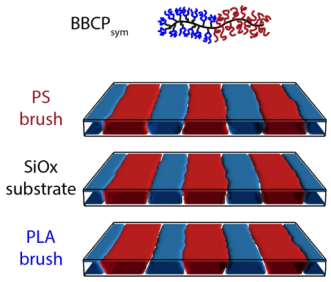

Figure 5. Simulation results presenting the details of the 3D domain shapes of BBCP$_{sym}$ on different substrates, showing the substrate effect on the PS domain shape. Domains were initially aligned by imposing an external field to facilitate observing the cross section perpendicular to the domain orientation.

the alternating striped pattern reflects a structure of standing lamellae, where the bases of the PLA lamellae are widened (Figure 5, middle panel). Support for this conclusion came from hydrolytic PLA degradation experiments, where the film self-assembled on SiOx partially peeled off the surface (Figure 6b), which indirectly evidences a high surface fraction of the PLA domains at the film/substrate interface. For comparison, the PLA domains of BBCP$_{sym}$ films annealed on PS degraded neatly, leaving a continuous, corrugated film consisting of the remaining PS domains (Figure 6a). As the tilted image shows, the PS domains exhibit a trapezoid cross-sectional shape,

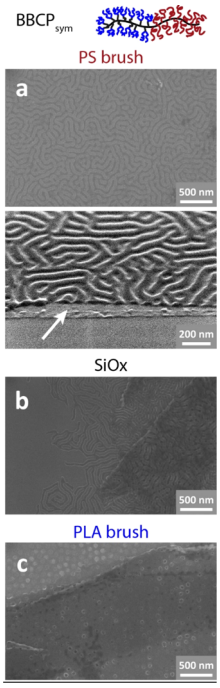

Figure 6. SEM images showing the ultrathin BBCP$_{sym}$ films cast on the three substrates after NaOH degradation of the PLA domains. (a) BBCP$_{sym}$ cast on the PS brush and annealed for 5 min, followed by PLA degradation. The bottom image shows the picture at a tilt of 55° near a scratch made in the film, which exposed the bare SiOx (bottom part) and the PS brush (white arrow), and confirms the complete degradation of the PLA domains. (b) BBCP$_{sym}$ cast on SiOx and annealed for 20 min, followed by PLA degradation. The film appeared torn and folded onto itself. (c) BBCP$_{sym}$ cast on the PLA brush and annealed for 5 min, followed by PLA degradation. The film features cylindrical-like pores and appears folded onto itself.

where the bases of the PS domains appear wider than the bases of the (etched) PLA domains, corroborating the simulation results (Figure 5, top panel).

The assembly of BBCP$_{sym}$ on the PLA brush revealed a unique intermediate morphology. After 5 min of annealing, the film presents a pattern of circular depressions surrounded by a matrix (Figure 3j). Similar structures are also captured by simulations at early times (Figure 4, bottom row). We attribute the depressions to PLA domains according to the AFM phase images, which show that the depressions are harder than the matrix. Hydrolytic degradation leaves cylindrical-like pores, which further corroborates this conclusion (Figure 6c). Upon further annealing, these dots evolve into elongated PLA stripes (Figure 3l).

This morphological behavior corroborates the conclusion that the initial response of the cast film is to follow the nature of the substrate. In this system, strongly antisymmetric wetting conditions prevail, which drive the PS grafts to the film surface and attract the PLA grafts to the substrate. Indeed, the average surface fraction of the PS domains at the free surface as calculated from the AFM images was 0.65 ± 0.08, which is higher than the volume fraction of the PS domains (f_{PS} = 0.57). This result is consistent with the structure simulated for this system, which shows a strong deviation from a rectangular cross section of the PS lamellae into an inverted trapezoid (Figure 5, bottom panel). It is possible that the increase in PS concentration at the free surface triggers a morphological transition to a cylindrical-like phase. We have recently shown that the phase diagram of backbone-symmetric PS−PLA BBCP is slightly asymmetric and shifted toward a low PS content, where the lamella-to-cylinder transition occurs around f_{PS} = 0.65.[34]

The initial 3D morphology is hypothesized as neck-like PLA domains embedded in the PS matrix. Han and co-workers have suggested the existence of a cone-like morphology in lamellar polystyrene-*block*-poly(methyl methacrylate) (PS-*b*-PMMA) films under ultraconfinement of the film thickness.[35] We have recently modeled the behavior of PS-*b*-PMMA copolymers under confinement and showed that the actual shape of the cross section of these features resembles a neck rather than a trapezoid. The formation of this nonbulk morphology was rationalized as arising from a combination of the thickness confinement and high substrate selectivity toward the domain forming the isolated features.[24] In the PS−PLA BBCP$_{sym}$ system studied here, this structure is transient and evolves into a lamellar-like morphology during annealing. This behavior can be attributed to the mixing of the PLA brush chains with the PLA side chains of the BBCP, which changes the compositional profile within the ultrathin film, and to the strong preference of BBCPs to form flat interfaces. Nonetheless, as the simulations show, the final morphology features PLA lamellae with widened bases (Figure 5, bottom panel) owing to the high selectivity of the PLA brush to the PLA domains. These structures represent a continuous progression of the morphology of BBCP$_{sym}$ on the different substrates from the PS brush (featuring narrow PLA bases) through SiOx (wider PLA bases) to the PLA brush (a further increase in PLA wetting and surface enrichment with PS domains).

To our knowledge, this is the first demonstration of a cylindrical-like morphology from a backbone-symmetric and graft-symmetric BBCP. This morphology is driven not by the tendency to minimize the PS−PLA interfacial area but by the wetting conditions. Although this morphology does not

https://dx.doi.org/10.1021/acs.macromol.0c02057
Macromolecules 2021, 54, 2079−2089

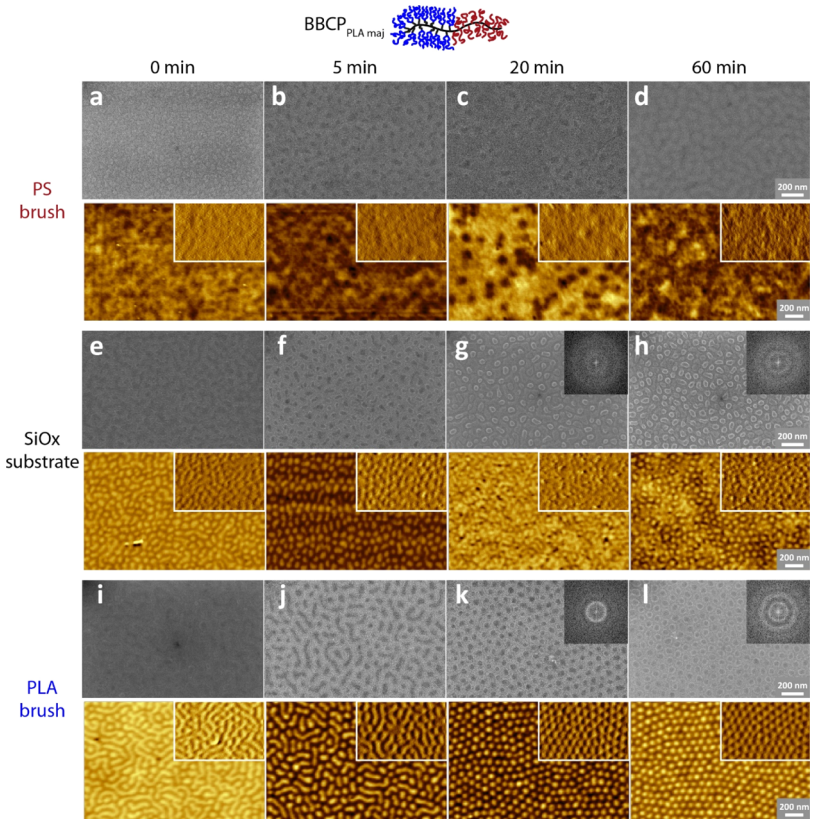

Figure 7. Self-assembly of $BBCP_{PLA\ maj}$ in ultrathin films on three different types of substrates. Top: SEM images; bottom: AFM height images. Insets in the AFM images: phase images corresponding to the same portion of the height image it overlaps. Insets of the SEM images (g,h,k,l): Fourier transform of the corresponding SEM images. AFM height *z*-scale: 15 nm.

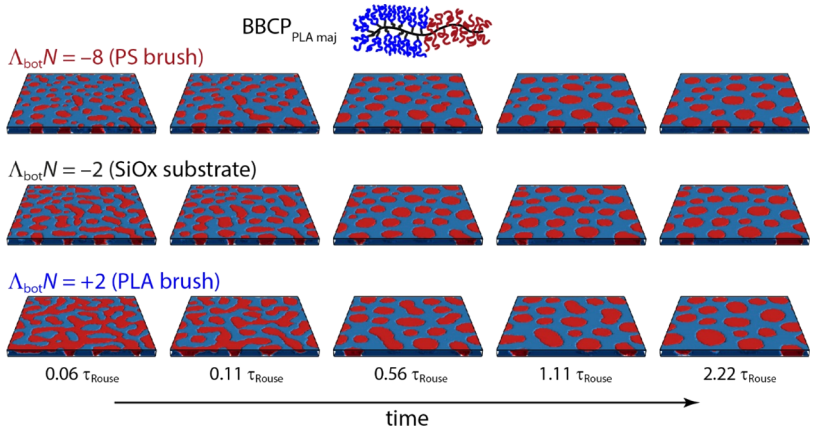

Figure 8. Simulation results showing the structure evolution in thin films of $BBCP_{PLA\ maj}$ on various substrates. The *A* and *B* components (PS and PLA domains) are colored red and blue, respectively.

represent a thermodynamic equilibrium, it could be easily arrested in briefly annealed films. The relatively large diameter of the pores formed after PLA degradation (~30−40 nm)—a direct outcome of the BBCP architecture—is hard to access using linear block copolymers. The ability to generate vertically orientated channels with such diameters in uniform ultrathin films is of tremendous technological importance as active layers of composite membranes for ultrafiltration applications.[36]

Self-Assembly of the Asymmetric BBCP. The obvious difference between $BBCP_{sym}$ and $BBCP_{PLA\ maj}$ is that the latter features PLA grafts that are longer than the PS grafts. When it comes to its self-assembly in ultrathin films on different substrates, the outcome is, however, not trivial.

The SEM images of ultrathin $BBCP_{PLA\ maj}$ assembled on the PS brush show that $BBCP_{PLA\ maj}$ initially gives rise to a pattern of dots that evolves into a worm-like structure (Figure 7a−d). The surface patterns that evolve in the simulations are somewhat similar, starting with small PS domains that coalesce into larger, somewhat elongated structures (Figure 8, top row). However, the AFM images do not exhibit any clear surface pattern at any annealing time (bottom images in Figure 7a−d). While this discrepancy between the AFM and SEM images is unclear, it could be attributed to the presence of a thin PLA

https://dx.doi.org/10.1021/acs.macromol.0c02057
Macromolecules 2021, 54, 2079−2089

overcoat formed by the long PLA side chains despite the slight selectivity of the THF vapor toward PS mentioned above. This is explained by a combination of the strong attraction of the PS-grafted blocks to the PS brush, which substantially depletes the free surface from PS, and the fact that PS is the minority component of $BBCP_{PLA\ maj}$.

The assembly of $BBCP_{PLA\ maj}$ on SiOx resulted in an initial structure of PS worms that evolved into protruding PS dots during annealing, as shown by microscopy and simulations (Figures 7e–h and 8, middle row). Both SEM and AFM images show similar patterns, which indicate that both domains exist at the film surface. The difference in the behavior of $BBCP_{PLA\ maj}$ on SiOx and on the PS-coated substrate is again attributed to the substrate chemistry. SiOx is slightly less attractive to the PS domains, and hence, the dot pattern of the annealed film on SiOx reflects the asymmetric composition of $BBCP_{PLA\ maj}$, in analogy to the striped pattern observed for the assembly of $BBCP_{sym}$ on SiOx (Figure 3h).

As has been discussed previously,[20] the shape of the isolated PS domains is of distorted cylinders, arising from the competition between the asymmetric composition that favors curved interfaces and the enhanced tendency of the stiff bottlebrush backbone for lamellar packing. Nonetheless, surface fraction analysis reveals that $\sigma_{PS} = 0.50$, which is considerably larger than the PS volume fraction ($f_{PS} = 0.32$). This analysis is in line with the interfacial energy considerations, which stipulate higher exposure of the PS domains at the surface of the film, and the reduced contact area of these domains with the SiOx substrate. Indeed, simulations of field-aligned systems reveal that the dots pattern observed at the film surface corresponds to PS domains that take the shape of inverted truncated cones, which increases the exposure of the PS domains at the free surface and reduces their contact area with the substrate (Figure 9, middle panel).

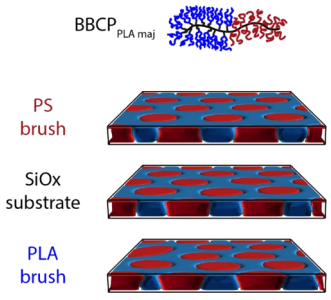

Figure 9. Simulation results presenting the details of the 3D domain shapes of $BBCP_{PLA\ maj}$ on different substrates, showing the substrate effect on the PS domain shape. Domains were initially aligned by imposing an external field to facilitate observing the cross section at the center of the PS domains.

The self-assembly of $BBCP_{PLA\ maj}$ on the PLA brush resembles that on SiOx owing to similar preference of these substrates for the PLA domains. However, the initial structure contains longer PS domains than those initially observed on SiOx (Figure 7i). More importantly, however, the annealed morphology presents a highly ordered hexagonal array of circular features, which are considerably more uniform in shape than the distorted features observed on SiOx (Figure 7l vs Figure 7h; see Fourier transform insets and circularity analysis in Figure S3). The Fourier transform analysis of the SEM image pattern is consistent with hexagonal symmetry. The calculated surface fraction of the PS domains in the annealed film is $\sigma_{PS} = 0.47$, which is much higher than the PS volume fraction in the BBCP. Simulation results show that the bases of the inverted truncated conical structures of the PS domains are much narrower than those for $BBCP_{PLA\ maj}$ assembled on SiOx (Figure 9, compare bottom and middle panels). The nature of such a high degree of domain ordering is unclear but could result from the higher repulsion of the PS domains from the PLA brush compared to the somewhat nonpreferential SiOx substrate.

Periodicity of the Self-Assembled Morphologies. The characteristic length scales of the different morphologies were extracted from the simulation results and compared to the experimental findings. The composition of the film was averaged along the substrate normal, z, and from it, we computed the structure factor of composition variations in the lateral dimension (Figure 10).

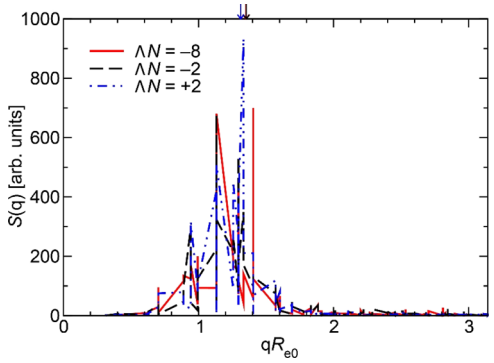

Figure 10. Structure factor, $S(q)$, of the composition of $BBCP_{sym}$ as a function of the magnitude of the lateral wave vector, $q = \sqrt{q_x^2 + q_y^2}$, calculated from the simulation results. Arrows denote the position of the average wave vector q.

Due to the lack of the long-range order of the morphology and the finite system size, the structure factor does not exhibit a single, well-defined peak. Therefore, we define a characteristic wave vector via the average, $\langle q \rangle = \sum_{|\mathbf{q}|<\pi/R_{e0}} |\mathbf{q}| S(\mathbf{q}) / \sum_{|\mathbf{q}|<\pi/R_{e0}} S(\mathbf{q})$, and the concomitant characteristic length scale by $L = 2\pi/\langle q \rangle$. These data are compiled in Table 3. For $BBCP_{sym}$, the ratio between the domain spacing in the experiment and the characteristic length scale extracted from the simulations is approximately independent from the type of the substrate. This allows us to identify the length scale of the simulation as $R_{e0} \approx 20$ nm. The same approximate mapping

Table 3. Comparison between the Characteristic Length Scales of the Morphology on Different Substrates, Observed in the Simulation and in the Experiment

	$BBCP_{sym}$			$BBCP_{PLA\ maj}$		
	L (sim.)	L (exp.) (nm)	R_{e0} (nm)	L (sim.)	L (exp.) (nm)	R_{e0} (nm)
$\Lambda N = -8$ (PS brush)	$4.65R_{e0}$	82	17.6	$3.89R_{e0}$	95	24.4
$\Lambda N = -2$ (SiOx)	$4.65R_{e0}$	89	19.1	$3.79R_{e0}$	73	19.3
$\Lambda N = +2$ (PLA brush)	$4.79R_{e0}$	93	19.4	$4.34R_{e0}$	78	18.0

https://dx.doi.org/10.1021/acs.macromol.0c02057
Macromolecules 2021, 54, 2079–2089

also applies to $BBCP_{PLA\ maj}$. The film thickness used in the simulation, $D = 0.85R_{e0}$, thus corresponds to about 12.8 nm, in good agreement with the experiment.

We note that the ratio between the average characteristic length scale, L, of the microphase separated morphology and the extension of the bottlebrush in the disordered thin film is rather large. For $BBCP_{sym}$, we obtain $\frac{L}{R_e} \approx \frac{4.70}{\sqrt{2.28}} \approx 3.11$, whereas the $BBCP_{PLA\ maj}$ system yields the ratio $\frac{L}{R_e} \approx \frac{4.01}{\sqrt{3.00}} \approx 2.31$. Thus, it is likely that the chosen value of $\chi N_{bb} = 36$ corresponds to rather large segregation strength.

CONCLUSIONS

We have investigated the morphologies evolving in ultraconfined films of bottlebrush block copolymers that have backbones of a similar length and variable side-chain lengths on different types of substrates. The results revealed high morphological sensitivity to the substrate selectivity in the regime of ultraconfined thicknesses while taking into account the unique attributes that result from the bottlebrush architecture. The wetting properties of the substrate influence the extent of domain exposure at both surfaces, leading to nonbulk structures with different surface patterns that are obtained in a reproducible and controlled fashion. The experimental observations of the surface pattern are corroborated by simulations that provide information about the 3D morphology.

One of the insights from this work is that the deposited film initially responds to the substrate selectivity and may give rise to unexpected transient morphologies in the course of self-assembly. In this sense, we observed a quasi-cylindrical morphology despite the polymer symmetric composition of both the backbone and its side chains. This is the first demonstration of a nonlamellar morphology obtained from a symmetric bottlebrush block copolymer. The morphology that is anticipated from the polymer composition evolves upon further annealing, yet it is slightly modified under the influence of the substrate.

Based on these insights, we now investigate the cooperative self-assembly of bottlebrush block copolymers with gold nanoparticles in ultraconfined films on different substrates. This study is underway and will be reported in due course.

EXPERIMENTAL SECTION

Materials. PS−PLA BBCPs were synthesized by a combination of controlled radical and ring-opening polymerizations as reported previously.[11] $BBCP_{sym}$: M_n = 1442 kDa, $Đ$ = 1.11 (assembly on SiOx) and M_n = 1259 kDa, $Đ$ = 1.15; $BBCP_{PLA\ maj}$: M_n = 2173 kDa, $Đ$ = 1.09; [see Table 1 and the Supporting Information, Figure S1, for gel permeation chromatography (GPC) and NMR analyses]. Oxide-terminated PS (PS−OH), M_n = 9.5 kDa, was synthesized by anionic polymerization under a nitrogen atmosphere as described previously.[37] The PLA homopolymer (poly(D,L-lactide) (M_n = 10 kDa, $Đ$ = 1.2) was purchased from Sigma-Aldrich and used as received.

Substrate Modification. Silicon wafers containing 4 nm thick native oxide were cleaned in NoChromix solution in H_2SO_4 for 24 h and then rinsed for 20 min in distilled water. To graft the polymer brushes, 1 wt % PS−OH solution in toluene and 1 wt % PLA in THF solution were spin-coated at 3000 rpm for 30 s onto hydrophilic silicon wafers, heated to 170 °C for 24 h, sonicated for 5 min in THF, rinsed in THF, and dried under vacuum for 1 h. The resulting brush thicknesses were 5 and 6 nm for the PS brush and PLA brush, respectively, according to ellipsometry. The water contact angles were 10° (SiOx), 89° (PS brush), and 68° (PLA brush); the CH_2I_2 contact angles were 27° (SiOx), 35° (PS brush), and 43° (PLA brush).

Film Preparation. Stock solutions of the BBCP (5 wt %) were prepared in toluene and were let to equilibrate overnight. Dilute solutions (~0.5 wt % for films cast on SiOx and 0.30−0.35 wt % for films cast on the brush-coated substrates) were prepared and let to equilibrate for 15 min. Spin coating at 3000 rpm for 30 s of the solutions yielded films with total film thicknesses of 15 ± 1 nm (including the brush thickness in the respective substrates).

Samples coated with the BBCP films were cut into six pieces, and each series of samples was annealed in a closed Petri dish under a saturated THF atmosphere for various intervals of time (0, 1, 5, 10, 20, and 60 min), after which they were rapidly quenched by fast removal from the solvent vapor chamber. All the experiments were performed on the same day to maintain constant ambient conditions. We note that all films remained smooth under these conditions (i.e., did not coarsen into islands and holes).

Basic Characterization. ^{1}H NMR spectra were recorded on a Varian INOVA-500 (500 MHz) spectrometer using $CDCl_3$ as a solvent. Size exclusion chromatography analyses were carried out on Viscotek's GPC Max and TDA 302 Tetra Detector array system equipped with two PLgel PolyPore columns (Polymer Laboratories, Varian Inc.) using THF as the mobile phase at 30 °C. The system was calibrated with 10 linear PS standards with molecular weights ranging from 1.2 × 10^6 to 500 g/mol. High-resolution SEM images of the films were obtained with a Sirion microscope (FEI Company) at a 5 kV acceleration voltage. AFM images were obtained using a Dimension 3100 scanning probe microscope with a NanoScope V controller, Veeco, Santa Barbara, CA, and were corrected by first-order flattening using the NanoScope Analysis Program (V1.40, Bruker). Film and brush thicknesses were determined by ellipsometry as well as by AFM scans across scratches made with tweezers in the films immediately after freezing in liquid nitrogen. Contact angle measurements were performed on a DataPhysics OCA 15EC instrument and analyzed by the SCA 20 software, with 3−4.5 μL droplets of water and 1.5−3 μL droplets of CH_2I_2.

AFM Image Analysis. The periodicity of the BBCPs was determined from the analysis of AFM images as reported previously.[20] Fourier transformation on 2 μm × 2 μm images (performed using ImageJ software[38]) was followed by radial integration of the 2D scattering image that was carried out using the FIT2D software.[39] Height histograms were obtained using the built-in Depth Analysis tool in the NanoScope Analysis Program. The areal fractions of the PS phase were calculated using ImageJ software. AFM height or phase images were first filtered with the mean averaging factor (a 2 pixel radius), and the pixel histograms were generated and deconvoluted to calculate the area under the Gaussians corresponding to the PS and PLA domains.

Simulations. To model the BBCPs, approximately four monomeric repeat units of a chemically realistic representation were mapped onto one coarse-grained segment. The reduction of the number of degrees of freedom and the soft interactions, with which the coarse-grained segments interact, allowed us to address the required large time and length scales.

The model BBCPs consisted of a linear backbone with N_{bb} = 72 coarse-grained backbone segments, divided equally between the blocks (chain length heterogeneity was not taken into account). The A and B segments, representing PS-grafted and PLA-grafted blocks, respectively, were assumed to have the same segmental volume and statistical segment length, b_0. Segments were connected by Gaussian springs with a mean-squared length, b_0^2. In the following, we measure all length scales in units of the root-mean-squared end-to-end distance, $R_{e0} = b_0(N_{bb} - 1)^{1/2}$, which the linear backbone without side chains adopts in a homogeneous melt. The numbers of side chains emanating from each A and B backbone segment are z_A = 4 and z_B = 8, respectively. This structure models the bifurcated architecture of the PLA-grafted block. The side-chain length of the PS block in both BBCPs is $N_{sc,A}$ = 9. Each B side chain is composed of $N_{sc,B}$ = 4 segments in $BBCP_{sym}$ and 8 segments in $BBCP_{PLA\ maj}$. The calculated values of f_A are 0.50 and 0.36 for $BBCP_{sym}$ and $BBCP_{PLA\ maj}$,

https://dx.doi.org/10.1021/acs.macromol.0c02057
Macromolecules 2021, 54, 2079−2089

respectively, which are close to the corresponding values of f_{PS} (Table 1). Thus, even in this coarse-grained description, $BBCP_{sym}$ contains 2520 segments and $BBCP_{PLA\ maj}$ comprises 3672 segments. The chain architectures are characterized using the "curly bracket" notation[40,41] as follows

$BBCP_{sym}$ $A(A\{9\})\{4\}\cdots\cdots\cdots B(B\{4\})\{8\}$ (36 times, 36 times)

$BBCP_{PLA\ maj}$ $A(A\{9\})\{4\}\cdots\cdots\cdots B(B\{8\})\{8\}$ (36 times, 36 times)

The number density, ρ_0, of segments in the melt of BBCPs is set to $\rho_0 R_{e0}^3 = 7119$ or $\rho b_0^3 \approx 11.9$. The bonded interactions take the form

$$\frac{\mathcal{H}_b}{k_B T} = \sum_{k=0}^{n} \sum_{i,j=1}^{N} \frac{A_{ij}}{2} \frac{3}{2b_0^2} [\mathbf{r}_{ki} - \mathbf{r}_{kj}]^2 \tag{2}$$

where n denotes the number of bottlebrush molecules and $\mathbf{r}_{ki}$ is the position of the ith segment on the bottlebrush polymer, k, and the value of A_{ij} is 1 between bonded segments and 0 otherwise.

The nonbonded interactions describe the near-incompressibility of the dense melt and the incompatibility between segment species, A and B

$$\frac{\mathcal{H}_{nb}}{k_B T} = \rho_0 \int d\mathbf{r} \left\{ -\frac{\chi}{4} [\hat{\phi}_A(\mathbf{r}) - \hat{\phi}_B(\mathbf{r})]^2 + \frac{\kappa}{2} [\hat{\phi}_A(\mathbf{r}) + \hat{\phi}_B(\mathbf{r}) - 1]^2 \right\} \tag{3}$$

where the Flory–Huggins parameter quantifies the repulsion between A and B segments, and we use the rather large value $\chi N_{bb} = 36$. The model parameter, κ, is related to the inverse isothermal compressibility, and we use the small value $\kappa N_{bb} = 50$ in our soft, coarse-grained model in accord with previous studies. The microscopic normalized number density of A segments is obtained from the explicit segment positions via

$$\hat{\rho}_A(r) = \frac{1}{\rho_0} \sum_{k=1}^{n} \sum_{i_A=1}^{N_A} \delta(\mathbf{r} - \mathbf{r}_{ki}) \tag{4}$$

where the sum over i_A enumerates all N_A segments of type A in a BBCP. The B density, $\hat{\rho}_B(\mathbf{r})$, is given by a similar expression. In the Monte Carlo simulations, the densities and the integral in eq 3 are evaluated on a collocation grid with a spacing of $\Delta L \approx R_{e0}/7$.

We consider a thin-film geometry $L \times L \times D$, where $L = 20R_{e0}$ is the lateral extension of the film. Periodic boundary conditions are applied in the two lateral directions, x and y. The film is confined by two hard, impenetrable walls that represent the substrate and the narrow surface to the vapor. The film thickness is $D = 0.85R_{e0}$. Such a film comprises $n = 960$ $BBCP_{sym}$ or 659 $BBCP_{PLA\ maj}$, that is, more than 2.4×10^6 coarse-grained segments.

The top surface in contact to the vapor exhibits a preference to the A component, that is, each A segment that is located at a distance ΔL away from the top surface changes the energy by $-5k_BT/N_{bb}$, corresponding to $\Lambda_{top}N_{bb} = -5$, whereas the presence of a B segment at this surface region increases the energy by the same amount. Additionally, the substrate exhibits a preference that also extends a distance ΔL into the film. We use the values $\Lambda_{bottom}N_{bb} = -8$, -2, and $+2$ to model a substrate coated with a PS brush, a SiOx substrate, and a PLA-coated substrate, respectively.

The simulations employed the single-chain-in-mean-field (SCMF) algorithm,[42] which exploits the separation between the strong but computationally inexpensive bonded interactions (eq 2) and the weak nonbonded interactions (eq 3). To this end, the weak and slowly varying nonbonded interactions are temporarily replaced with external fields that are recalculated after each MCS from the explicit segment coordinates. This quasi-instantaneous field approximation is the analogue of RESPA[43] in molecular dynamics simulations and captures fluctuation and correlation effects. Thus, in contrast to self-consistent field theory,[12] SCMF simulations capture the correlation hole in the intermolecular pair correlation function[42] that gives rise to corrections to the Gaussian chain behavior of linear macromolecules in a melt and the stretching of bottlebrushes.[30] The SCMF algorithm allows for an efficient implementation on graphics processing units; we typically employ 4 NVIDIA V100 to simulate a system.[40]

Segment positions were updated using a force-biased local Monte Carlo algorithm[44] resulting in Rouse-like dynamics.[45] The thin films were equilibrated at $\kappa N_{bb} = 50$ and $\chi N_{bb} = 0$ and no surface preference for more than 10^7 MCS, where each segment was attempted to move on average once in an MCS. Then, the system was quenched to $\chi N_{bb} = 36$ and the preference of the substrate and solvent–vapor surface was accounted for, and we monitored the kinetics of structure formation.

■ ASSOCIATED CONTENT

Supporting Information

The Supporting Information is available free of charge at https://pubs.acs.org/doi/10.1021/acs.macromol.0c02057.

GPC curves and NMR spectra of the BBCPs; AFM thickness profile across a scratch in the film of $BBCP_{sym}$ assembled on the PS brush; determination of surface energies of the substrates; assessment of SiOx selectivity toward PS and PLA; and circularity analysis of the PS domains as they appear in the SEM images of $BBCP_{PLA\ maj}$ films annealed on SiOx and the PLA brush (PDF)

■ AUTHOR INFORMATION

Corresponding Authors

Marcus Müller − *Institute for Theoretical Physics, Georg-August-University Göttingen, Göttingen 37077, Germany;* orcid.org/0000-0002-7472-973X; Email: mmueller@theorie.physik.uni-goettingen.de

Javid Rzayev − *Department of Chemistry, University at Buffalo, The State University of New York, Buffalo, New York 14260-3000, United States;* orcid.org/0000-0002-9280-1811; Email: jrzayev@buffalo.edu

Roy Shenhar − *Institute of Chemistry and the Center for Nanoscience and Nanotechnology, The Hebrew University of Jerusalem, Jerusalem 9190401, Israel;* orcid.org/0000-0002-0631-1542; Email: roys@huji.ac.il

Authors

Yaron Aviv − *Institute of Chemistry and the Center for Nanoscience and Nanotechnology, The Hebrew University of Jerusalem, Jerusalem 9190401, Israel*

Esra Altay − *Department of Chemistry, University at Buffalo, The State University of New York, Buffalo, New York 14260-3000, United States*

Ofer Burg − *Institute of Chemistry and the Center for Nanoscience and Nanotechnology, The Hebrew University of Jerusalem, Jerusalem 9190401, Israel*

Complete contact information is available at: https://pubs.acs.org/10.1021/acs.macromol.0c02057

Author Contributions

The manuscript was written through contributions of all authors. All authors have given approval to the final version of the manuscript.

https://dx.doi.org/10.1021/acs.macromol.0c02057
Macromolecules 2021, 54, 2079−2089

Funding
Financial support for this work was provided by the Israel Science Foundation (grant number 229/17), the National Science Foundation (DMR-1709371), and Deutsche Forschungsgemeinschaft (MU 1674/16-2).

Notes
The authors declare no competing financial interest.

■ ACKNOWLEDGMENTS

The authors thank Elina Ploshnik for a sample of the PS−OH brush and Yousef Farraj for assistance with contact angle measurements. Y.A. thanks the Hebrew University for a doctoral fellowship. M.M. acknowledges computing time granted by the John von Neumann Institute for Computing (NIC), Germany, provided on the supercomputer JUWELS at the Jülich Supercomputing Center (JSC) as well as computational resources at HLRN Göttingen/Berlin and GWDG Göttingen.

■ REFERENCES

(1) Sheiko, S. S.; Sumerlin, B. S.; Matyjaszewski, K. Cylindrical Molecular Brushes: Synthesis, Characterization, and Properties. *Prog. Polym. Sci.* **2008**, *33*, 759−785.
(2) Verduzco, R.; Li, X.; Pesek, S. L.; Stein, G. E. Structure, Function, Self-Assembly, and Applications of Bottlebrush Copolymers. *Chem. Soc. Rev.* **2015**, *44*, 2405−2420.
(3) Rzayev, J. Molecular Bottlebrushes: New Opportunities in Nanomaterials Fabrication. *ACS Macro Lett.* **2012**, *1*, 1146−1149.
(4) Wintermantel, M.; Schmidt, M.; Tsukahara, Y.; Kajiwara, K.; Kohjiya, S. Rodlike Combs. *Macromol. Rapid Commun.* **1994**, *15*, 279−284.
(5) Wintermantel, M.; Gerle, M.; Fischer, K.; Schmidt, M.; Wataoka, I.; Urakawa, H.; Kajiwara, K.; Tsukahara, Y. Molecular Bottlebrushes. *Macromolecules* **1996**, *29*, 978−983.
(6) Runge, M. B.; Dutta, S.; Bowden, N. B. Synthesis of Comb Block Copolymers by Romp, Atrp, and Rop and Their Assembly in the Solid State. *Macromolecules* **2006**, *39*, 498−508.
(7) Rathgeber, S.; Pakula, T.; Wilk, A.; Matyjaszewski, K.; Beers, K. L. On the Shape of Bottle-Brush Macromolecules: Systematic Variation of Architectural Parameters. *J. Chem. Phys.* **2005**, *122*, 124904.
(8) Dalsin, S. J.; Hillmyer, M. A.; Bates, F. S. Linear Rheology of Polyolefin-Based Bottlebrush Polymers. *Macromolecules* **2015**, *48*, 4680−4691.
(9) Hu, M.; Xia, Y.; McKenna, G. B.; Kornfield, J. A.; Grubbs, R. H. Linear Rheological Response of a Series of Densely Branched Brush Polymers. *Macromolecules* **2011**, *44*, 6935−6943.
(10) Vlassopoulos, D.; Fytas, G.; Loppinet, B.; Isel, F.; Lutz, P.; Benoit, H. Polymacromonomers: Structure and Dynamics in Nondilute Solutions, Melts, and Mixtures. *Macromolecules* **2000**, *33*, 5960−5969.
(11) Rzayev, J. Synthesis of Polystyrene-Polylactide Bottlebrush Block Copolymers and Their Melt Self-Assembly into Large Domain Nanostructures. *Macromolecules* **2009**, *42*, 2135−2141.
(12) Dalsin, S. J.; Rions-Maehren, T. G.; Beam, M. D.; Bates, F. S.; Hillmyer, M. A.; Matsen, M. W. Bottlebrush Block Polymers: Quantitative Theory and Experiments. *ACS Nano* **2015**, *9*, 12233−12245.
(13) Gai, Y.; Song, D.-P.; Yavitt, B. M.; Watkins, J. J. Polystyrene-Block-Poly(Ethylene Oxide) Bottlebrush Block Copolymer Morphology Transitions: Influence of Side Chain Length and Volume Fraction. *Macromolecules* **2017**, *50*, 1503−1511.
(14) Gu, W.; Huh, J.; Hong, S. W.; Sveinbjornsson, B. R.; Park, C.; Grubbs, R. H.; Russell, T. P. Self-Assembly of Symmetric Brush Diblock Copolymers. *ACS Nano* **2013**, *7*, 2551−2558.
(15) Yavitt, B. M.; Gai, Y.; Song, D.-P.; Winter, H. H.; Watkins, J. J. High Molecular Mobility and Viscoelasticity of Microphase-Separated Bottlebrush Diblock Copolymer Melts. *Macromolecules* **2017**, *50*, 396−405.
(16) Sveinbjornsson, B. R.; Weitekamp, R. A.; Miyake, G. M.; Xia, Y.; Atwater, H. A.; Grubbs, R. H. Rapid Self-Assembly of Brush Block Copolymers to Photonic Crystals. *Proc. Natl. Acad. Sci. U.S.A.* **2012**, *109*, 14332−14336.
(17) Runge, M. B.; Bowden, N. B. Synthesis of High Molecular Weight Comb Block Copolymers and Their Assembly into Ordered Morphologies in the Solid State. *J. Am. Chem. Soc.* **2007**, *129*, 10551−10560.
(18) Xia, Y.; Olsen, B. D.; Kornfield, J. A.; Grubbs, R. H. Efficient Synthesis of Narrowly Dispersed Brush Copolymers and Study of Their Assemblies: The Importance of Side-Chain Arrangement. *J. Am. Chem. Soc.* **2009**, *131*, 18525−18532.
(19) Bolton, J.; Bailey, T. S.; Rzayev, J. Large Pore Size Nanoporous Materials from the Self-Assembly of Asymmetric Bottlebrush Block Copolymers. *Nano Lett.* **2011**, *11*, 998−1001.
(20) Aviv, Y.; Altay, E.; Fink, L.; Raviv, U.; Rzayev, J.; Shenhar, R. Quasi-Two-Dimensional Assembly of Bottlebrush Block Copolymers with Nanoparticles in Ultrathin Films: Combined Effect of Graft Asymmetry and Nanoparticle Size. *Macromolecules* **2019**, *52*, 196−207.
(21) Knoll, A.; Horvat, A.; Lyakhova, K. S.; Krausch, G.; Sevink, G. J. A.; Zvelindovsky, A. V.; Magerle, R. Phase Behavior in Thin Films of Cylinder-Forming Block Copolymers. *Phys. Rev. Lett.* **2002**, *89*, 035501.
(22) Daoulas, K. C.; Müller, M.; Stoykovich, M. P.; Park, S. M.; Papakonstantopoulos, Y. J.; de Pablo, J. J.; Nealey, P. F.; Solak, H. H. Fabrication of Complex Three-Dimensional Nanostructures from Self-Assembling Block Copolymer Materials on Two-Dimensional Chemically Patterned Templates with Mismatched Symmetry. *Phys. Rev. Lett.* **2006**, *96*, 036104.
(23) Li, W.; Liu, M.; Qiu, F.; Shi, A.-C. Phase Diagram of Diblock Copolymers Confined in Thin Films. *J. Phys. Chem. B* **2013**, *117*, 5280−5288.
(24) Michman, E.; Langenberg, M.; Stenger, R.; Oded, M.; Schvartzman, M.; Müller, M.; Shenhar, R. Controlled Spacing between Nanopatterned Regions in Block Copolymer Films Obtained by Utilizing Substrate Topography for Local Film Thickness Differentiation. *ACS Appl. Mater. Interfaces* **2019**, *11*, 35247−35254.
(25) Brassat, K.; Lindner, J. K. N. Nanoscale Block Copolymer Self-Assembly and Microscale Polymer Film Dewetting: Progress in Understanding the Role of Interfacial Energies in the Formation of Hierarchical Nanostructures. *Adv. Mater. Interfaces* **2019**, *7*, 1901565.
(26) Imre, B.; Renner, K.; Pukanszky, B. Interactions, Structure and Properties in Poly(Lactic Acid)/Thermoplastic Polymer Blends. *eXPRESS Polym. Lett.* **2014**, *8*, 2−14.
(27) Vayer, M.; Hillmyer, M. A.; Dirany, M.; Thevenin, G.; Erre, R.; Sinturel, C. Perpendicular Orientation of Cylindrical Domains Upon Solvent Annealing Thin Films of Polystyrene-B-Polylactide. *Thin Solid Films* **2010**, *518*, 3710−3715.
(28) Sheiko, S. S.; Gerle, M.; Fischer, K.; Schmidt, M.; Möller, M. Wormlike Polystyrene Brushes in Thin Films. *Langmuir* **1997**, *13*, 5368−5372.
(29) Hong, S. W.; Gu, W.; Huh, J.; Sveinbjornsson, B. R.; Jeong, G.; Grubbs, R. H.; Russell, T. P. On the Self-Assembly of Brush Block Copolymers in Thin Films. *ACS Nano* **2013**, *7*, 9684−9692.
(30) Paturej, J.; Sheiko, S. S.; Panyukov, S.; Rubinstein, M. Molecular Structure of Bottlebrush Polymers in Melts. *Sci. Adv.* **2016**, *2*, No. e1601478.
(31) Sunday, D. F.; Chremos, A.; Martin, T. B.; Chang, A. B.; Burns, A. B.; Grubbs, R. H. Concentration Dependence of the Size and Symmetry of a Bottlebrush Polymer in a Good Solvent. *Macromolecules* **2020**, *53*, 7132−7140.
(32) Biresaw, G.; Carriere, C. J. Compatibility and Mechanical Properties of Blends of Polystyrene with Biodegradable Polyesters. *Composites, Part A* **2004**, *35*, 313−320.
(33) It should be noted that usually the domain that is more compatible with the solvent features lower film thickness than the less

https://dx.doi.org/10.1021/acs.macromol.0c02057
Macromolecules 2021, 54, 2079−2089

compatible domain (because it retains the solvent longer during the evaporation stage). The reversal of this behavior with the BBCP films is attributed to the lower mobility of the grafted PS side chains compared to the segments in a linear block copolymer. The morphology apparently stands for a quenched state that represents the higher degree of swelling of the PS-grafted blocks in solution.

(34) Jiang, L.; Nykypanchuk, D.; Pastore, V. J.; Rzayev, J. Morphological Behavior of Compositionally Gradient Polystyrene−Polylactide Bottlebrush Copolymers. *Macromolecules* **2019**, *52*, 8217−8226.

(35) Xuan, Y.; Peng, J.; Cui, L.; Wang, H.; Li, B.; Han, Y. Morphology Development of Ultrathin Symmetric Diblock Copolymer Film Via Solvent Vapor Treatment. *Macromolecules* **2004**, *37*, 7301−7307.

(36) Baruth, A.; Seo, M.; Lin, C. H.; Walster, K.; Shankar, A.; Hillmyer, M. A.; Leighton, C. Optimization of Long-Range Order in Solvent Vapor Annealed Poly(Styrene)-Block-Poly(Lactide) Thin Films for Nano Lithography. *ACS Appl. Mater. Interfaces* **2014**, *6*, 13770−13781.

(37) Pavan, M. J.; Ploshnik, E.; Shenhar, R. Nanoparticle Assembly on Topographical Polymer Templates: Effects of Spin Rate, Nanoparticle Size, Ligand, and Concentration. *J. Phys. Chem. B* **2012**, *116*, 13922−13931.

(38) Rasband, W. S. *ImageJ*, version 1.39u; U.S. National Institutes of Health: Bethesda, MD, 1997−2014; http://imagej.nih.gov/ij/.

(39) Hammersley, A. P.; Svensson, S. O.; Hanfland, M.; Fitch, A. N.; Hausermann, D. Two-Dimensional Detector Software: From Real Detector to Idealised Image or Two-Theta Scan. *High Pressure Res.* **1996**, *14*, 235−248.

(40) Schneider, L.; Müller, M. Multi-Architecture Monte-Carlo (Mc) Simulation of Soft Coarse-Grained Polymeric Materials: Soft Coarse Grained Monte-Carlo Acceleration (SOMA). *Comput. Phys. Commun.* **2019**, *235*, 463−476.

(41) Lin, T.-S.; Coley, C. W.; Mochigase, H.; Beech, H. K.; Wang, W.; Wang, Z.; Woods, E.; Craig, S. L.; Johnson, J. A.; Kalow, J. A.; Jensen, K. F.; Olsen, B. D. Bigsmiles: A Structurally-Based Line Notation for Describing Macromolecules. *ACS Cent. Sci.* **2019**, *5*, 1523−1531.

(42) Daoulas, K. C.; Müller, M. Single Chain in Mean Field Simulations: Quasi-Instantaneous Field Approximation and Quantitative Comparison with Monte Carlo Simulations. *J. Chem. Phys.* **2006**, *125*, 184904.

(43) Tuckerman, M.; Berne, B. J.; Martyna, G. J. Reversible Multiple Time Scale Molecular-Dynamics. *J. Chem. Phys.* **1992**, *97*, 1990−2001.

(44) Rossky, P. J.; Doll, J. D.; Friedman, H. L. Brownian Dynamics as Smart Monte-Carlo Simulation. *J. Chem. Phys.* **1978**, *69*, 4628−4633.

(45) Müller, M.; Daoulas, K. C. Single-Chain Dynamics in a Homogeneous Melt and a Lamellar Microphase: A Comparison between Smart Monte Carlo Dynamics, Slithering-Snake Dynamics, and Slip-Link Dynamics. *J. Chem. Phys.* **2008**, *129*, 164906.

https://dx.doi.org/10.1021/acs.macromol.0c02057
Macromolecules 2021, 54, 2079−2089